

***Final Draft***  
**of the original manuscript:**

Ma, S.; Yuan, H.:

**A continuum damage model for multi-axial low cycle fatigue of  
porous sintered metals based on the critical plane concept**

In: *Mechanics of Materials* (2016) Elsevier

DOI: [10.1016/j.mechmat.2016.09.013](https://doi.org/10.1016/j.mechmat.2016.09.013)

# A continuum damage model for multi-axial low cycle fatigue of porous sintered metals based on the critical plane concept

Songyun Ma <sup>a</sup> Huang Yuan <sup>b,\*</sup>

<sup>a</sup>*Institute of Materials Research, Helmholtz Research Center Geesthacht, Germany*

<sup>b</sup>*School of Aerospace Engineering, Tsinghua University, Beijing, China*

---

## Abstract

Experimental investigations reveal very different damage mechanisms in porous sintered metals from those of conventional dense materials. Interactions between the inherent porosity and heterogeneous matrix result in complicated deformation behavior and fatigue damage processes. In the present work, the damage evolution in the sintered metal under multi-axial cyclic loading conditions is studied experimentally and computationally. The total damage is divided into the stress-related elastic damage, the plastic damage induced by the plastic deformations and the fatigue damage driven by cyclic loading. To predict the cyclic deformation behavior as well as the fatigue damage evolution, a nonlinear fatigue damage model coupled with the critical plane concept is proposed, embedded into the Ohno-Wang cyclic plasticity and implemented into the FEM software ABAQUS based on an implicit integration algorithm. The proposed damage model is computationally and experimentally verified under multi-axial cyclic loading paths with different strain amplitudes. A good agreement between experimental and computational results shows that the present model is able to describe cyclic mechanical behavior and fatigue damage of porous metals.

*Key words:* Porous sintered metal, cyclic damage evolution, cyclic plasticity, fatigue damage, fatigue life

---

## 1 Introduction

Sintered metals with more than 7% porosity exhibit different progressive degradation processes of mechanical properties compared to conventional dense metals [11]. The pre-existing porosity caused by the manufacturing process affects the damage evolution process substantially. Recently, numerous sintered steels with high mechanical strength are developed and regarded as

---

\* Corresponding author. Email: huang.yuan@tsinghua.edu.cn

promising candidates to replace the conventional dense metals, especially for automobile industry [3, 29]. To apply these materials for highly loaded parts, it is of importance to quantify the mechanical property and the damage accumulation process under various loading conditions.

The interaction between the inherent porosity and heterogeneous matrix results in complicated deformation and damage mechanisms in sintered metals. The fraction, size, distribution and morphology of voids in sintered metals directly affect their mechanical properties [34]. For the complexity in inelastic deformations and damage mechanisms, limited works on damage modeling of sintered metals have been published. In fact, different damage mechanisms can be found in sintered metals [9]. Under monotonic loading, experimental and computational investigation reveal that damage in sintered metal nucleates in macroscopic elastic stress state and develops with plastic deformations [30]. Consequently, the total damage can be decomposed into elastic damage and plastic damage. The elastic damage nucleates at a very low stress amplitude and dominated by the effective Mises stress, while the plastic damage is induced by the plastic strain [33]. Therefore, the damage evolution law should be appropriately proposed with respect to the physical interpretation of different damage mechanisms.

The GTN model is popular for modeling damage process in porous solids. Cedergren et al. [5] extended the GTN model with viscoplastic formulation and combined hardening model to investigate the damage accumulation of the sintered steel with 5.5% porosity under cyclic loading condition with different loading frequency. An unrealistic prediction result was obtained using the extended GTN model. Schneider et al. [26] used the GTN model for notched specimens and concluded that due to the high initial porosity the GTN model cannot be directly used for sintered metals. More recently, Ma et al. [22] proposed a continuum damage model to describe the mechanical behavior and the damage evolution under multi-axial monotonic loading paths. The model considered both damage at elastic stage and plastic damage. The simulation results were computationally and experimentally verified under multi-axial loading conditions. However, major published works are focused on damage under monotonic loading. The damage models for monotonic loadings cannot be directly employed for fatigue due to different damage mechanisms.

In general, fatigue failure is commonly observed in mechanical components and structures which are subjected to repeated loads [13]. The damage accumulation process under cyclic loadings is different from that under monotonic loading. Many works have been devoted to describe and quantify the fatigue damage process [1, 8, 17, 23, 35]. The most popular damage accumulation law was proposed by Palmgren and Miner with a simple linear function [28]. The Palmgren-Miner rule assumes a constant work absorption per loading cycle independently of the loading level by neglecting loading interaction. The model is widely used in the industry due to its simple formulation and implementation, although the linear damage accumulation law has strong limitations [24]. Many nonlinear damage evolution laws were proposed in order to consider effects observed in metal fatigue, such as load sequence, multi-axiality, and non-linearity of damage accumulation etc. [4, 14, 19]. Within the frame of continuum damage mechanics, Chaboche proposed a nonlinear cumulative fatigue damage model for predicting fatigue life in uniaxial loading case [6]. The Chaboche fatigue damage model is a stress-based model and includes effects of the mean stress and loading sequence on the damage process.

Desmorat et al. [12] introduced a mean-stress-dependent damage evolution law to describe the fatigue damage process under general complex loading. All the mentioned models are not suitable for porous sintered metals due to different damage mechanisms, as observed in the monotonic loading cases [21, 27].

To address the fatigue life prediction of components subjected to multi-axial loading conditions, the critical plane concept was proposed [20, 25, 31]. The concept is based on a physical interpretation of the fatigue process and experimental observations of nucleation and growth of cracks during loading [28]. Jiang [15] proposed a critical plane model for predicting fatigue life of material which is able to consider general cracking behavior, i.e. tensile and shear cracking of material under fatigue loadings. The application of the critical plane model has achieved great successes in predicting fatigue life under the multi-axial stress state [28]. However, the critical plane model does not involve a nonlinear damage evolution law as well as the effect of fatigue damage on the constitutive behavior of material.

In sintered metals, the fraction of porosity, the pore size, the pore shape and the pore spacing are all important factors influencing fatigue behavior [29]. Obviously, the porosity is not suitable to describe fatigue damage under repeated loads, since no significant growth of voids can be observed in experiments under cyclic loadings. At the macro scale, many investigations intended to relate the fatigue strength of the material with Young's modulus, yield stress and ultimate tensile strength [2, 3]. However, the published models cannot be directly employed for characterizing the nonlinear damage evolution in sintered metals, as reported for monotonic loading damage [22, 33], and accounting for the interaction between fatigue damage and mechanical response. A proper fatigue damage model has to be able to describe the damage accumulating process and reflect the influence of the strain amplitude on the fatigue life under multi-axial loading conditions. Generally speaking, the fatigue damage evolution for sintered metals is still an open issue. According to the best knowledge of the authors, there is no published paper on modeling elastic-plastic fatigue damage in porous sintered metals.

In the present work, the fatigue damage evolution was investigated experimentally and computationally. Experiments including monotonic loading and fatigue tests under different tension-torsion loading paths should provide the fundamental for establishing a fatigue damage evolution law. Based on the experimental observation and computational analysis, an elastic-plastic fatigue damage model by using the critical plane concept is proposed in the framework of continuum damage mechanics. The proposed fatigue damage evolution law is coupled with the Ohno-Wang cyclic plasticity model to predict the accumulation process of fatigue damage under multi-axial loading condition. The corresponding computational algorithm as well as FEM implementation are presented in the present work. Identification of material parameters is discussed. Finally, the proposed fatigue model is validated under different proportional loading paths. Computational results are discussed and compared with experimental results. It is confirmed that the present damage model can characterize multi-axial fatigue damage in sintered metals properly.

## 2 Uniaxial cyclic damage experiments

### 2.1 Material and specimen

To investigate the fatigue damage evolution process of sintered metals, the pure iron powder (atomized Hoeganaes ASC.100.29) from Hoeganaes Corporation was used to produce specimens with density  $7.2\text{g/cm}^3$ . The microstructure of sintered metals is characterized by the randomly distributed pores with irregular form, as shown in Fig. 1, which induce the strain localization in the microstructure scale and result in different mechanical behavior in comparison to conventional dense metals.

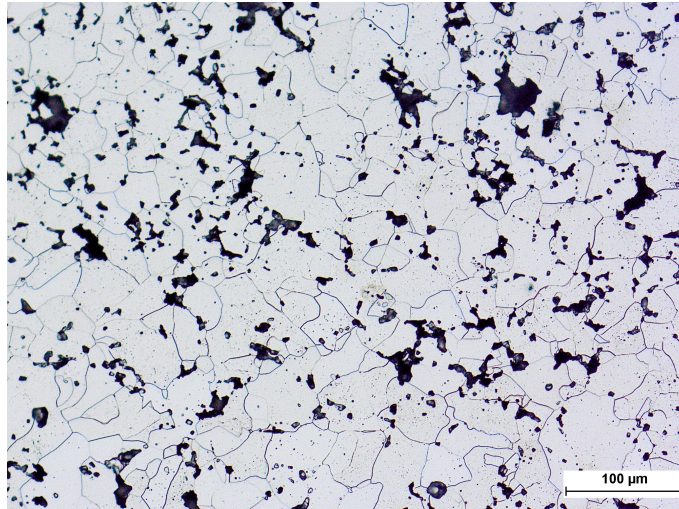


Figure 1. Microstructure of the sintered iron ASC.100.29 with the density  $7.2\text{g/cm}^3$ .

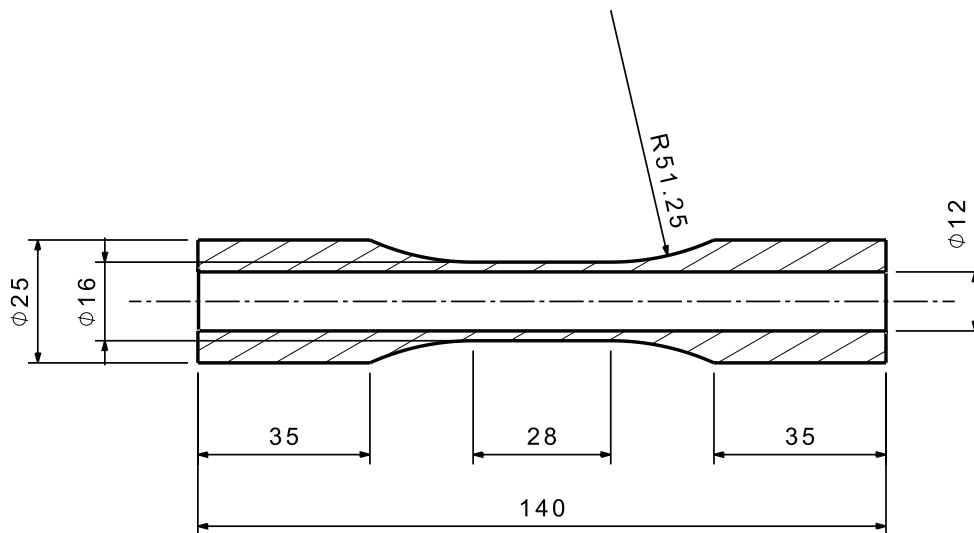


Figure 2. Geometry of the tubular tension-torsion specimen.

The strain-controlled fatigue tests with fully reversed tension-compression loadings were conducted on sintered iron tubular specimens. The thin-walled tubular specimen, as shown in Fig. 2, is used for testing under the tension-torsion cyclic loading conditions. The fatigue experiments were accomplished in the MTS-809 axial-torsional servo-hydraulic testing system. The MTS axial-torsional extensometer with 25 mm gage length was attached to the tubular specimen for the measurement of the axial and shear strains in the gage section. The extensometer has a range of +4% to -2% axial strain and  $\pm 5^\circ$  torsional rotation angle.

## 2.2 SEM observation of failure mechanisms

Qualitative SEM (Scanning Electron Microscope) examinations were performed in order to investigate the fatigue mechanisms. In the monotonic loading case, ductile dimples can be observed in necks between sintered powder particles [22]. Interconnections of micropores in the sintered neck regions contain significant high stress concentrations and lead to final fracture of the specimen [27]. Fractography shows that the microscopic damage mechanisms of fatigue differ from those of monotonic loading rupture significantly. In Fig. 3 the fractography of the fatigue specimen subjected to a strain amplitude 0.007 is illustrated. Under fatigue loading, localized fatigue striations are apparent, as shown in Fig. 3(b). Both ductile dimples and fatigue striations are present on the fatigue surface. The localized dimples indicate ductile fracture and are significantly less for the fatigue case with strain amplitude than that under monotonic loading.

The transgranular fracture in sintered metals was only observed in fatigue (Fig. 3(b)). The irregular pores induce additional stress concentrations and cause subcritical crack growth into particles, as observed from striations in Fig. 3(b). The transgranular failure is a known damage mechanism in dense metals, but only observed in fatigue in sintered metals. Under monotonic loading micro-cracks initiated near pores and propagated along powder particle boundaries due to high stress concentrations, i.e. the failure is dominated by the intergranular fracture, as shown in Fig. 3(c), which was taken from fatigue specimen, either. The experimental observation confirms that the damage mechanisms under cyclic loading are significantly different from those under monotonic loading. The material damage under fatigue loadings is significantly resulted from subcritical fracture mechanisms, which cannot be described by the damage models for monotonic loading cases [21, 33].

## 2.3 Experimental results

To quantify the fatigue damage, the approach suggested by Ma and Yuan [21, 33] is employed based on the recorded stress-strain hysteresis loops under cyclic loading. Following the damage definition of Kachanov [19], the material damage under uniaxial loading can be defined based

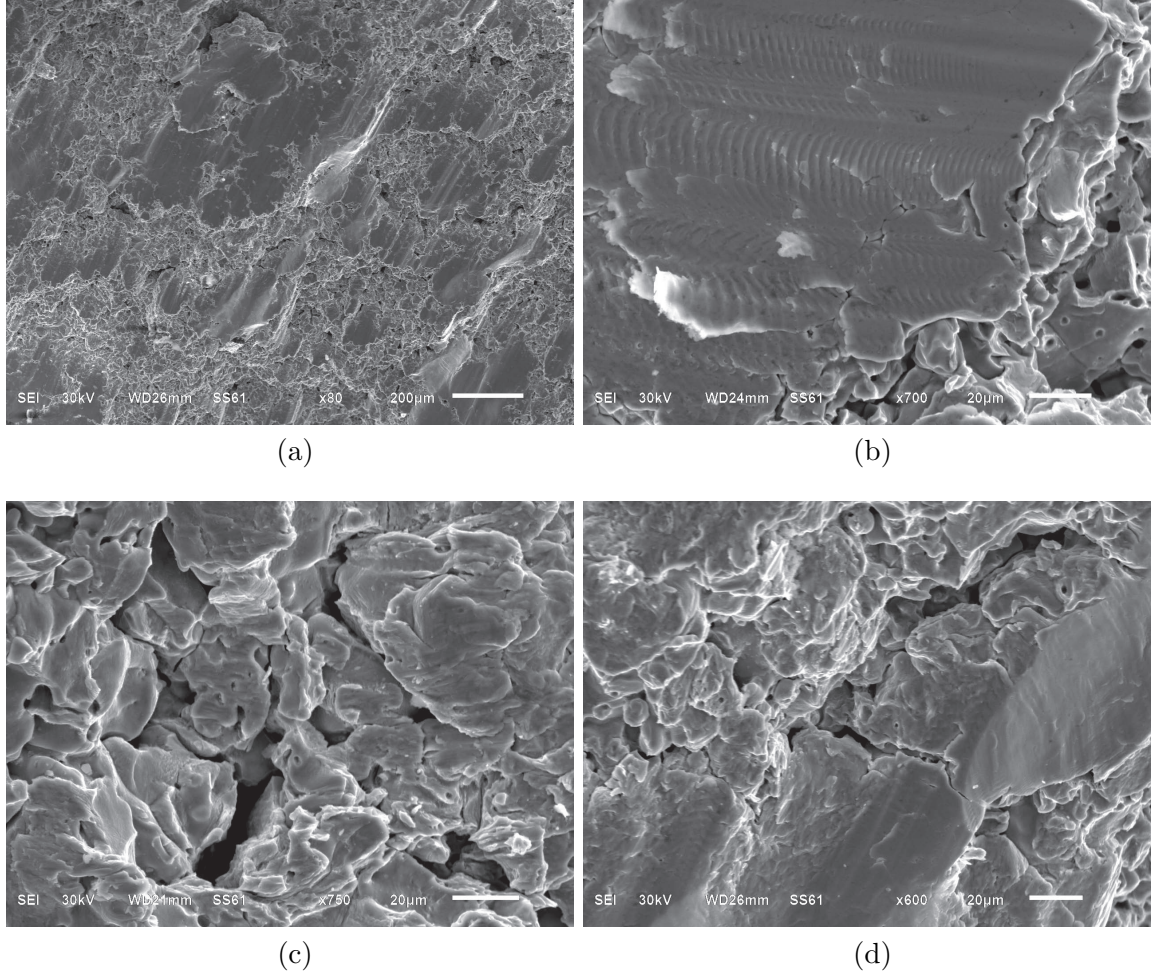


Figure 3. Differing from the fracture under monotonic loading, fatigue specimens show striations in the fracture surface. (a) Overview of the specimen fracture surface. (b) The transgranular fracture through particles with clear fatigue striations. (c) Intergranular fracture. (d) Mixture of the both fracture mechanisms.

on the variation of elastic modulus, as

$$D = 1 - \frac{E}{E_0}, \quad (1)$$

where  $E_0$  is the initial elastic modulus.  $E$  denotes the actual elastic modulus of the material depending on material degradation. The damage denotes the degradation of the material stiffness. Under multi-axial loading condition it can be calculated from the principal strain direction, as discussed in [33]. For cyclic fatigue cases the current elastic modulus can be obtained from the stress-strain loop. The elastic modulus is measured in the region of unloading, as shown in Fig. 4(a). Figure 4(b) shows variations of the actual elastic modulus with loading cycles in the strain-controlled uniaxial testing with different strain amplitudes. The test shows that the elastic modulus decreases continuously during cyclic loading, regardless of loading amplitudes. Note the initial elastic modulus  $E_0$  has been determined to be in the range of 155-165 GPa for the present sintered iron ASC.100.29. The reduction of elastic modulus can be

divided into three successive stages: The first stage with a dramatic decrease occurring during the first few cycles is followed by a stable regime with a constant decrease rate, which builds the major part of loading cycles. Finally, a rapid decrease of elastic modulus is observed before rupture, where crack coalescence occurs and the material becomes unstable. As expected, the loadings with higher strain amplitudes significantly accelerate the degradation process of the elastic property of sintered metals.

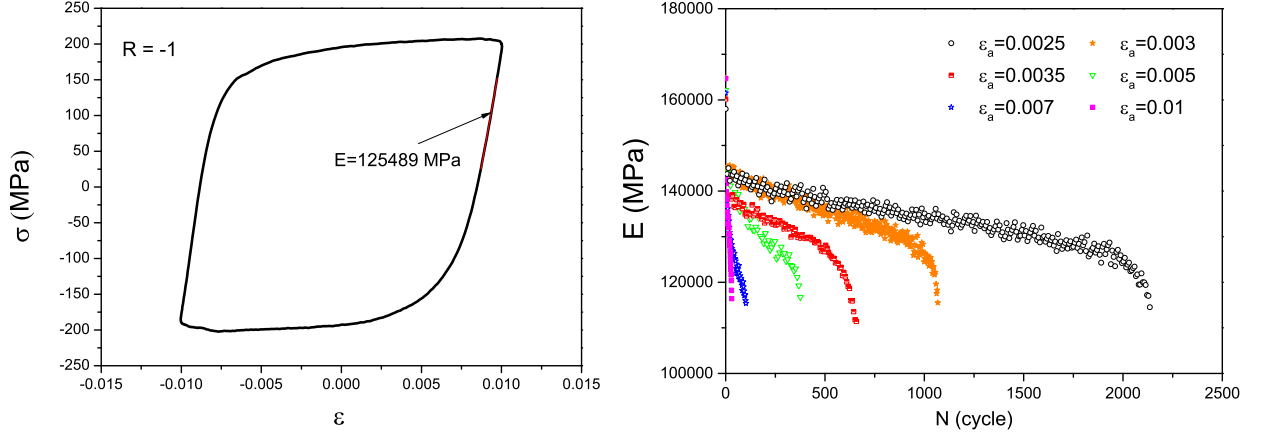


Figure 4. Measurement of elastic modulus in a stress-strain hysteresis loop under strain-controlled cyclic loading. (a) Actual elastic modulus is measured from the unloading range in a stress-strain loop. (b) Variations of elastic modulus as a function of loading cycles.

Figure 5(a) illustrates the damage evolution in the uniaxial cases with different strain amplitude according to Eq. (1). In the figure the total damage is plotted in course of loading cycles. The damage in the first loading cycle is the result of the monotonic elastic-plastic damage, which can be described by the model introduced by Ma and Yuan [21,33]. Experimental observations reveal that damage in the sintered metal initiates at a very low stress level under monotonic loading [21]. In the uniaxial compression test as shown in Fig. 6(a), a significant material degradation is found, which cannot be related to the plastic damage driven by void growth

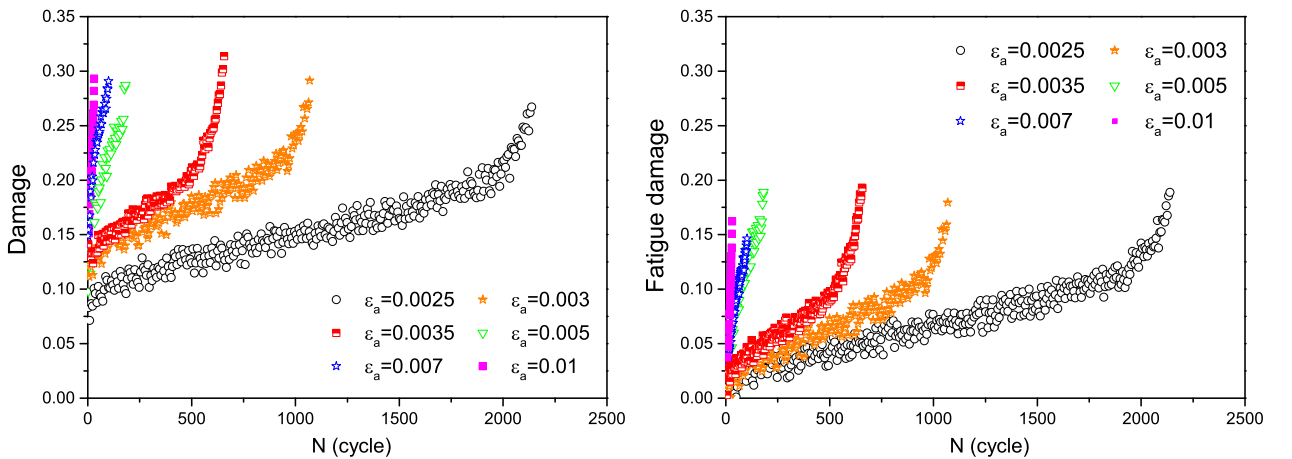


Figure 5. Damage evolution along the loading cycles identified in uniaxial fatigue tests with different strain amplitudes. (a) The total damage. (b) The fatigue damage based on Eq. (3).

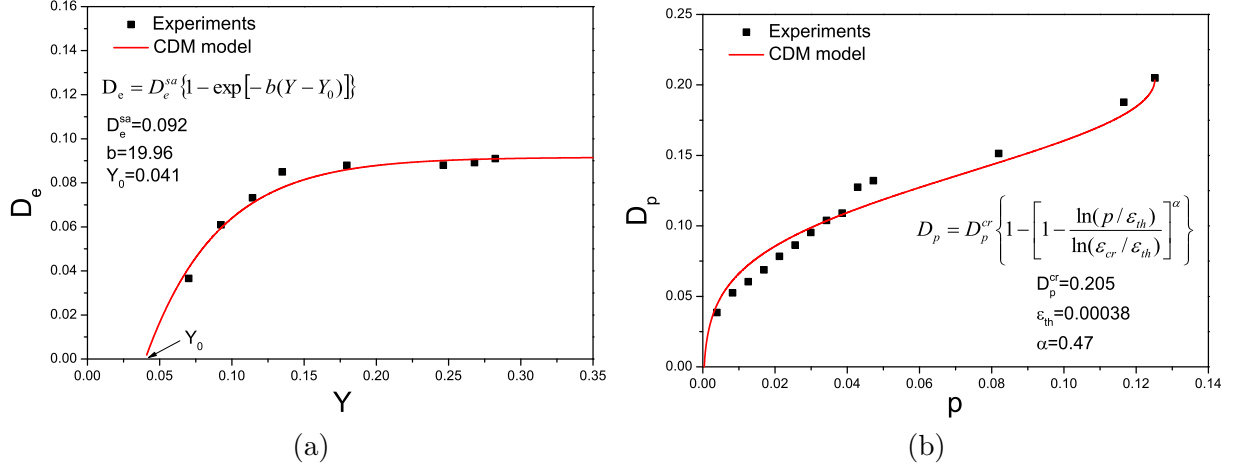


Figure 6. Decoupling the total damage into the elastic and plastic damage under monotonic uniaxial loading (a) Evolution of the elastic damage versus energy release rate in the uniaxial compression test. (b) Plastic damage evolution versus the plastic strain in the tensile test.

during plastic deformation. In addition, the damage occurs before yielding in the tension test (Fig. 6(b)). Therefore, The damage under monotonic loading is decoupled into elastic and plastic damage parts,  $\dot{D}_{ep} = \dot{D}_e + \dot{D}_p$ . Based on the evolution law of elastic damage ( $D_e$ ) identified in the uniaxial compression test, the plastic damage part ( $D_p$ ) can be separated from the total monotonic loading damage measured in the uniaxial tensile test as shown in Fig. 6(b) [21]. The total damage involves three damage contributions for general loading cases: Elastic damage driven by the monotonically increasing stress, plastic damage driven by the plastic deformation and fatigue damage due to the fluctuating loading, that is,

$$\dot{D} = \dot{D}_e + \dot{D}_p + \dot{D}_f. \quad (2)$$

The three damage terms denote three different damage mechanisms. The elastic damage  $D_e$  denotes damage under monotonic loading and will not grow without increase of the stress amplitude in the proposed damage model as suggested by Ma and Yuan [21]. Extensive experiments confirm the significant damage occurring under the elastic state in the sintered metal. With macroscopic plastification, the material is further degraded by the plastic strain, that is, the plastic damage  $D_p$  can grow, once the current effective equivalent Mises stress,  $\tilde{\sigma}_{eq} = \sqrt{3s_{ij}s_{ij}}/2/(1 - D)$ , is larger than the recorded maximum effective equivalent Mises stress in the whole loading history,  $\tilde{\sigma}_{eq}^{\max} = \max(\tilde{\sigma}_{eq}, t)$ . Here  $s_{ij}$  denotes the deviatoric stress tensor. The Einstein's summation convention is adopted.

Both elastic damage and plastic damage represent the monotonic loading damages, while the fatigue damage is related only to cyclic loading. The fatigue damage should not appear in the first half loading cycle and can only accumulate when the load repeats. In addition, the stress amplitude becomes quickly stable after several cycles under strain-controlled loading [27]. Therefore, it is reasonable to neglect the effect of cyclic hardening to the monotonic loading damage and to assume that the elastic damage and plastic damage can only accumulate in the first half cycle under strain-controlled cyclic loading, where fatigue damage is not activated.

Based on the above simplification, the fatigue damage during cyclic loading can be separated from the total damage in experiments by

$$D_f = D - D_{ep}, \quad (3)$$

where  $D_{ep}$  is the sum of elastic and plastic damage accumulated in the first half cycle, characterizing the monotonic loading path. Fig. 5(b) shows the variation of the fatigue damage,  $D_f$  versus the number of loading cycles based on Eq. (3). One learns from the figure that the fatigue damage evolution in sintered metals differs from that of conventional dense metals substantially. In most dense metals the fatigue damage nucleates after amount of loading cycles and grows gradually, so that the mechanical parts have a life period without damage. In addition, the damage rate of most dense metals is mainly monotonic to loading cycle and the damage accelerates after fatigue damage initiation [6]. The sintered metals show a very different evolution process which consists of three stages: The damage increases rapidly within few cycles characterized by convex curves in the  $D_f - N$  diagram, and then grows gradually at a stable phase due to the stable propagation of fatigue micro cracks. Finally, the damage develops dramatically and material loses its loading capacity in the last cycles, since micro cracks reach their critical lengths and the specimen fails. It is observed in Fig. 5(b) that the damage values at the rupture are in the range of 0.15 - 0.20. The critical damage is empirically defined with the average value of 0.18.

### 3 The cyclic elastic-plastic damage mechanics model

#### 3.1 Cyclic plasticity

It is known that metals under cyclic loading display special mechanical properties, such as Bauschinger effect, cyclic hardening/softening, non-Masing behavior, non-proportional hardening etc., which are not able to be considered within the conventional plasticity [28]. During last decades, a lot of efforts is devoted to develop unified comprehensive constitutive models of cyclic plasticity [7, 16, 25]. The multi-linear kinematic hardening model proposed by Ohno and Wang [18], in which the backstress has a critical state for dynamic recovery, is widely used to describe the cyclic behavior under different loading cases and has been validated for various materials. The introduction of a critical state and a power function for each dynamic recovery term enables the Ohno-Wang model to provide good predictions of uniaxial ratcheting [10]. For these reasons, the Ohno-Wang cyclic plasticity model is employed to coupled with the isotropic damage variable for modeling the inelastic deformation and damage behavior of sintered metals under cyclic loading.

Based on the hypothesis of the strain equivalence [19], the effective stress acting on the effective configuration,  $\tilde{\sigma}_{ij}$ , is defined as

$$\tilde{\sigma}_{ij} = \frac{\sigma_{ij}}{1 - D}, \quad (4)$$

where  $D$  is the isotropic damage variable for representing the degradation state of material. Within the framework of the small deformation, the total strain rate is divided into elastic and plastic parts, as

$$\dot{\epsilon}_{ij} = \dot{\epsilon}_{ij}^e + \dot{\epsilon}_{ij}^p.$$

The isotropic elastic Hooke's law reads

$$\epsilon_{ij}^e = \frac{1 + \nu}{E_0} \tilde{\sigma}_{ij} - \frac{\nu}{E_0} \tilde{\sigma}_{kk} \delta_{ij},$$

with  $\delta_{ij}$  as Kronecker delta. In the current damaged configuration it becomes

$$\epsilon_{ij}^e = \frac{1 + \nu}{E_0} \frac{\sigma_{ij}}{1 - D} - \frac{\nu}{E_0} \frac{\sigma_{kk} \delta_{ij}}{1 - D}, \quad (5)$$

where  $E_0$  and  $\nu$  are the elasticity constants in the initial material.

The yield function for cyclic plasticity coupled with the isotropic damage variable is defined as

$$F = \tilde{\sigma}_e - \sigma_y = \sqrt{\frac{3}{2} \frac{(s_{ij} - \alpha_{ij})(s_{ij} - \alpha_{ij})}{(1 - D)(1 - D)}} - \sigma_y = 0 \quad (6)$$

with the definition of the effective equivalent stress

$$\tilde{\sigma}_e = \sqrt{\frac{3}{2} \frac{(s_{ij} - \alpha_{ij})(s_{ij} - \alpha_{ij})}{(1 - D)(1 - D)}},$$

where  $s_{ij}$  and  $\alpha_{ij}$  are the deviatoric stress and the backstress tensor, respectively.  $\sigma_y$  represents the initial yield stress of the material. As experimentally investigated in [27], the peak stress becomes quickly stable after few cycles under strain-controlled cyclic loading. Therefore, the isotropic hardening part for describing the transient hardening/softening behavior of material is neglected in the present work.

The backstress  $\alpha_{ij}$  is composed of  $M$  components in the Ohno-Wang kinematic hardening model [18], as

$$\alpha_{ij} = \sum_{k=1}^M \alpha_{ij}^{(k)}. \quad (7)$$

The dynamic recovery is only fully active when the magnitude

$$\bar{\alpha}^{(k)} = \left( \frac{3}{2} \alpha_{ij}^{(k)} : \alpha_{ij}^{(k)} \right)^{1/2} \quad (8)$$

reaches the critical value  $r^{(k)}$ . The critical state of dynamic recovery is represented by a surface defined as

$$f^{(k)} = \left( \bar{\alpha}^{(k)} \right)^2 - \left( r^{(k)} \right)^2. \quad (9)$$

With the Heaviside step function  $H$ , the evolution equation of the backstress  $\alpha_{ij}^{(k)}$  is expressed in the following form

$$\dot{\alpha}_{ij}^{(k)} = \zeta^{(k)} \left[ \frac{2}{3} r^{(k)} \dot{\epsilon}_{ij}^p - H(f^{(k)}) \dot{p} \alpha_{ij}^{(k)} \right]. \quad (10)$$

Above  $\zeta^{(k)}$  is the material parameter in the linear part of the evolution equations. The rate of equivalent plastic strain is defined as

$$\dot{p} = \sqrt{\frac{2}{3} \dot{\epsilon}_{ij}^p \dot{\epsilon}_{ij}^p}. \quad (11)$$

The plastic strain rate is obtained by using the flow rule,

$$\dot{\epsilon}_{ij}^p = \dot{\lambda} \frac{\partial F}{\partial \sigma_{ij}}.$$

By introducing the maximum effective equivalent stress as memory stress of material in the loading history from time 0 to the current time  $t$ ,  $\tilde{\sigma}_{eq}^{\max}$ . The rate of the equivalent plastic strain contributes either to the accumulation of the equivalent plastic strain under monotonic loading,  $p_m$ , or to the accumulation of the equivalent plastic strain from cyclic loading,  $p_f$ , as

$$\dot{p} \Rightarrow \begin{cases} \dot{p}_m & \tilde{\sigma}_{eq} > \tilde{\sigma}_{eq}^{\max}, \\ \dot{p}_f & \tilde{\sigma}_{eq} \leq \tilde{\sigma}_{eq}^{\max}. \end{cases} \quad (12)$$

The accumulative equivalent plastic strain is then

$$p_m = \int \dot{p}_m dt, \quad p_f = \int \dot{p}_f dt. \quad (13)$$

In other words, these two accumulation processes of the equivalent plastic strains,  $p_m$  and  $p_f$ , cannot be activated simultaneously.

## 3.2 Damage evolution law

### 3.2.1 Elastic and plastic damage under monotonic loading

The elastic damage evolution law and plastic damage evolution law under monotonic loading in [21, 33] are summarized here briefly. The evolution equation of the elastic damage is driven by stress and expressed as exponential function of  $Y$

$$\dot{D}_e = D_e^{sa} b \exp[-b \langle Y - Y_0 \rangle] \dot{Y}. \quad (14)$$

Obviously, the elastic damage is characterized by the initial damage resistance,  $Y_0$ , the parameter  $b$  and the saturation damage  $D_e^{sa}$ .  $Y_0$  and  $D_e^{sa}$  describe nucleation and the upper limit of the damage, which were reported in [21, 33]. In the thermodynamics framework of continuum damage mechanics, the damage driving force  $Y$  is derived by differentiating the proposed Helmholtz free energy density with respect the damage. With the assumption that the damage is only coupled with the elastic strain energy density in the Helmholtz free energy density [19],

the strain energy density release rate  $Y$  can be expressed as

$$Y = \frac{1}{2} \tilde{\sigma}_{ij} \epsilon_{ij}^e = \frac{\tilde{\sigma}_{eq}^2}{2E_0} f(\eta), \quad (15)$$

where  $\epsilon_{ij}^e$  is the elastic strain tensor.  $\tilde{\sigma}_{eq} = \sqrt{3/2(s_{ij}s_{ij})}/(1-D)$  is the Mises stress. Substituting the Hooke's law into Eq. (15), one obtains the explicit expression of the stress triaxiality dependence of the strain energy release rate, as

$$f(\eta) = \frac{2}{3}(1 + \nu) + 3(1 - 2\nu)\eta^2. \quad (16)$$

The elastic damage depends on the stress triaxiality explicitly.

The plastic damage  $D_p$  increases, only when the new plastic loading occurs, that is, the equivalent stress under current loading  $\sigma_{eq}$  is larger than the recorded maximum equivalent stress  $\sigma_{eq}^{\max}$  of the whole loading history ( $\sigma_{eq} > \sigma_{eq}^{\max}$ ). The plastic damage is activated when the effective accumulated plastic strain  $p_m$  reaches the threshold strain  $\epsilon_{th}$  for the positive hydrostatic stress ( $\sigma_H \geq 0$ ), that is,

$$\dot{D}_p = \begin{cases} 0 & \text{if } p_m < \epsilon_{th} \text{ or } \sigma_H < 0, \\ \frac{Y}{S_0} \frac{(D_p^{cr} - D_p)^{(\beta-1)/\beta}}{p_m^{(2+n)/n}} \dot{p}_m & \text{if } p_m \geq \epsilon_{th} \text{ and } \sigma_H \geq 0, \end{cases} \quad (17)$$

where  $S_0$  is the material damage parameter,  $n$  is the plastic hardening exponent in the monotonic Ramberg-Osgood model,  $\beta$  is the damage exponent that determines the shape of the damage evolution law.

The proposed evolution laws of the elastic and plastic damage are applied to the sintered iron with the density  $7.2\text{g/cm}^3$ . Fig. 6 shows the comparison between the experimental and computational results under monotonic uniaxial loading. It is seen that the proposed elastic and plastic damage model provides an accurate description of the damage process under monotonic loading. More details about the damage model and results for monotonic loading are found in [21, 22, 33].

### 3.2.2 Fatigue damage

From multi-axial fatigue analysis the fatigue damage is related to the maximum stress as well as the strain amplitude [28]. Generally, a fatigue damage model should consider the four aspects as follows: (i) the physical fatigue damage mechanisms; (ii) the nonlinear accumulation of fatigue damage; (iii) The mean-stress or stress ratio effect on the fatigue damage; (iv) the loading sequence effect due to the material memory of previous loading history [12, 28]. In the present fatigue damage model the critical plane concept is adopted to formulate the fatigue damage evolution equation, since the critical plane concept is based on a physical mechanisms of the nucleation and growth of cracks and widely accepted for evaluating the multiaxial fatigue life [31].

From works of Jiang etc. [15,32] the fatigue damage is proportional to the plastic strain energy. By extending the Bonora model [4] to fatigue damage with the plastic strain energy as driving force, the new fatigue damage evolution equation for fatigue damage can be written as

$$\dot{D}_f = \frac{\tilde{\sigma}_{eq}^{\max}}{\sigma_f} \frac{(D_f^{cr} - D_f)^{(\alpha-1)/\alpha}}{p_f^w} \frac{1}{S_f} \dot{W}^{\max}, \quad (18)$$

where  $\sigma_f$  denotes the tensile strength from the monotonic tensile experiment. The parameters  $\alpha$ ,  $w$  and  $S_f$  in Eq. (18) are material parameters.  $\tilde{\sigma}_{eq}^{\max}$  is the maximum effective Mises stress in the whole loading history for considering the load sequence effect on evolution of fatigue damage. The additional influences from the current damage state as well as the accumulated effective plastic strain are included in the fatigue damage evolution. The term  $(D_f^{cr} - D_f)^{(\alpha-1)/\alpha}$  in Eq. (18) considers different shapes of the nonlinear damage evolution curves and will be discussed later. Additionally,  $p_f$  is the accumulative plastic strain under cyclic loading defined in Eq. (13). The power-law form of the plastic strain,  $p_f^w$ , takes into account the influence of the accumulated plastic deformation under cyclic loading on the fatigue damage process.

The fatigue damage is directly related to  $\dot{W}^{\max}$ , the maximum value of the plastic strain energy density rate  $\dot{W}$  at the critical plane [15,32]. Obviously  $\dot{W}$  is not an invariant and depends on the orientation angles  $\theta$  and  $\phi$  as shown in Fig. 7 with the normal direction  $\mathbf{n}$ .  $\theta$  is the angle between the projection of unit vector  $\mathbf{n}$  on the  $xy$  plane and the  $x$ -axis whereas  $\phi$  is the angle between the unit vector  $\mathbf{n}$  and the  $z$ -axis. The plastic strain energy rate is evaluated at the plane with the normal direction  $\mathbf{n}$ , as

$$\dot{W}(\theta, \phi) = a\tilde{\sigma}\epsilon^p + \frac{1-a}{2}\tilde{\tau}\dot{\gamma}^p, \quad (19)$$

where  $\epsilon^p$  and  $\dot{\gamma}^p$  represent plastic strains corresponding to the effective normal stress  $\tilde{\sigma}$  and shear stress  $\tilde{\tau}$  on the critical plane, respectively. It is noted that two shear components exist on the plane. In Eq. (19),  $\tilde{\tau}$  and  $\dot{\gamma}^p$  are the maximum values of the shear components,  $\tilde{\tau} = \max\{\tilde{\sigma}_{1'3'}, \tilde{\sigma}_{1'2'}\}$  and  $\dot{\gamma}^p = \max\{\dot{\epsilon}_{1'3'}^p, \dot{\epsilon}_{1'2'}^p\}$ .  $a$  is a model parameter related to the fatigue cracking behavior, ranging from 0 to 1. When  $0 < a < 0.37$ , the criterion can predict shear dominated failure process. When  $a \geq 0.5$ , the tensile cracking behavior is predicted. Mixed cracking behavior can be taken into consideration by choosing  $a$  between 0.37 and 0.5 [15].

The critical plane is defined as the plane experiencing the maximum value of  $\dot{W}(\theta, \phi)$ . The orientation of the critical plane,  $(\theta^{cr}, \psi^{cr})$ , can be determined by rotating the plane and evaluating the maximum value of the strain energy rate as

$$\dot{W}^{\max}(\theta^{cr}, \psi^{cr}) = \max\{\dot{W}(\theta, \phi)\}, \quad (20)$$

where  $\theta$  and  $\phi$  are the orientation angles of the unit normal vector  $\mathbf{n}$  of the rotated plane as shown in Fig. 7.

The effective stress and strain tensor can be transformed as

$$\tilde{\sigma}'_{kl} = m_{ki}\tilde{\sigma}_{ij}m_{lj}, \quad d\epsilon'_{kl} = m_{ki}d\epsilon_{ij}^p m_{lj}, \quad (21)$$

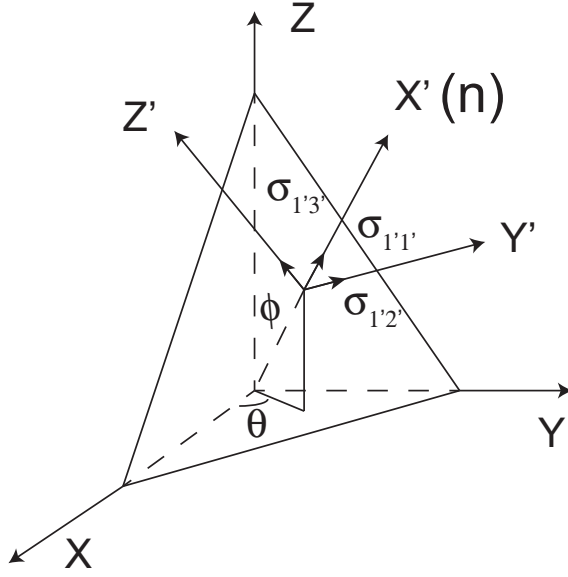


Figure 7. Rotating a plane in a three dimensional coordinate system.

where the transformation tensor for a given set of angles  $\theta$  and  $\phi$  is expressed as

$$m_{ij} = \begin{bmatrix} \cos \theta \sin \phi & \sin \theta \sin \phi & \cos \phi \\ -\sin \theta & \cos \theta & 0 \\ -\cos \theta \cos \phi & -\sin \theta \cos \phi & \sin \phi \end{bmatrix}. \quad (22)$$

The proposed elastic-plastic damage model has to be implemented in the FEM software ABAQUS via the user subroutine UMAT using an implicit integration algorithm. The return mapping algorithm is used to update the internal state variables and stresses for the given strain increment.

#### 4 Fatigue damage model under uniaxial cyclic loading

In order to derive an analytical solution of fatigue damage evolution for the uniaxial reversal cyclic loading case ( $R_\epsilon = \epsilon_{\min}/\epsilon_{\max} = -1$ ), the following assumptions are made: (a) The variation of the damage variable  $D$  during one cycle is so small that  $D_f$  within one loading cycle is supposed to be constant; (b) The transient cyclic hardening or softening with the first few cycles is ignored. The accumulated plastic strain energy on the critical plane within one cycle can be calculated by  $\Delta W = \int dW^{\max}$ . The accumulated plastic strain within  $N$  stable cycles can be estimated by  $p_f = 4N\epsilon_p^a$ , where  $\epsilon_p^a$  is the plastic strain amplitude of cyclic loading.

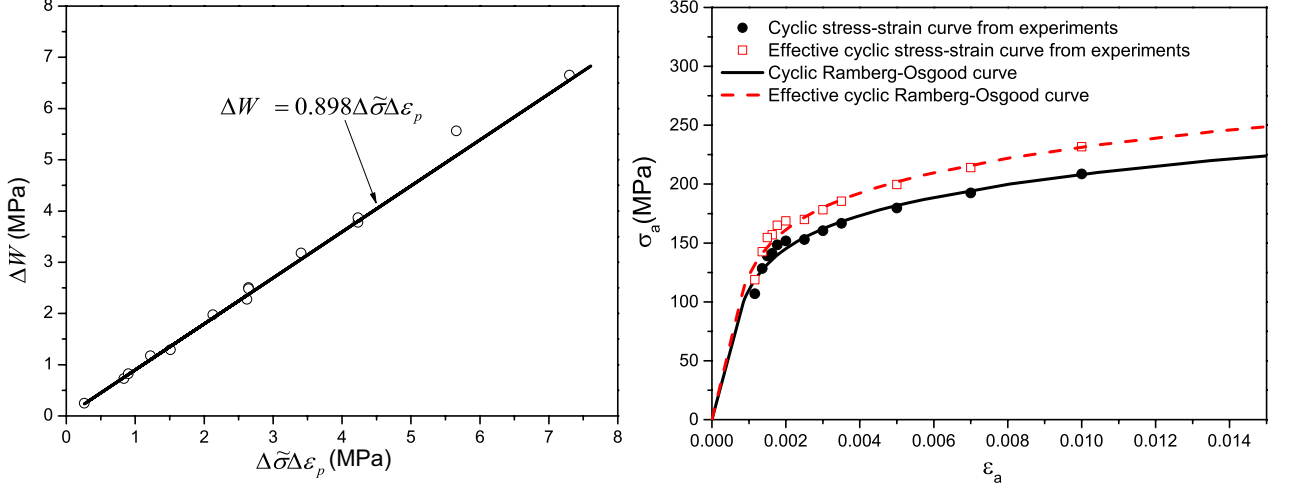


Figure 8. Characterization of fatigue damage in the sintered iron. (a) Correlation between the plastic strain energy on the critical plane within one cycle  $\Delta W$  and the product of the effective stress and strain ranges  $\Delta\tilde{\sigma} \Delta\epsilon_p$ . (b) Cyclic stress-strain curves in the current damaged and effective configuration.

Then, the fatigue damage evolution for one cycle can be written as

$$\frac{dD_f}{dN} = \frac{\tilde{\sigma}_a (D_f^{cr} - D_f)^{(\alpha-1)/\alpha}}{\sigma_f (4N\epsilon_p^a)^w} \frac{1}{S_f} \Delta W, \quad (23)$$

where  $\tilde{\sigma}_a$  is the effective stress amplitude.

For calculating the accumulated plastic strain energy on the critical plane in one cycle,  $\Delta W$ , one needs a proper cyclic plasticity model to describe the cyclic deformation behavior of material. Alternatively,  $\Delta W^{\max}$  can be calculated based on the stress-strain loop of the stable cycle of experiments. Based on the experimental data, the calculated plastic strain energy per cycle  $\Delta W$  is plotted versus the product of stress range and plastic strain range  $\Delta\tilde{\sigma}$  and  $\Delta\epsilon_p$  ( $\Delta\tilde{\sigma} = 2\tilde{\sigma}^a$  and  $\Delta\epsilon_p = 2\epsilon_p^a$ ). In Fig. 8(a), it is shown that  $\Delta W$  can be approximated by a linear equation

$$\Delta W = \bar{\omega} \Delta\tilde{\sigma} \Delta\epsilon_p, \quad (24)$$

where  $\bar{\omega}$  is a factor in the linear equation, which is 0.898 for sintered iron with density  $7.2\text{g/cm}^3$ , as shown in Fig. 8(a). Note that the effective stress can be calculated from Eqs. (1) and (4), by giving nominal stress values. By using the Masing postulate, the relationship between the plastic strain amplitude  $\epsilon_a^p$  and the stress amplitude  $\tilde{\sigma}_a$  can be described by the effective cyclic stress-strain equation in a power-law, as

$$\epsilon_a^p = \left[ \frac{\tilde{\sigma}_a}{K'} \right]^{1/n'}, \quad (25)$$

as shown in Fig. 8(b). Substituting Equations (25) and (24) into (23), one obtains

$$\frac{dD_f}{dN} = \frac{2^{2-w} \bar{\omega} K'^2}{S_f \sigma_f} (D_f^{cr} - D_f)^{(\alpha-1)/\alpha} (\epsilon_a^p)^{2n' - w + 1} (2N)^{-w} \quad (26)$$

Integrating Eq. (26), we have

$$-\alpha(D_f^{cr} - D_f)^{\frac{1}{\alpha}} = A(\epsilon_a^p)^{2n' - w + 1}(2N)^{1-w} + C, \quad (27)$$

where  $C$  is a constant depending on boundary conditions and  $A$  is defined by

$$A = \frac{2^{2-w}\bar{\omega}K^2}{2(1-w)S_0\sigma_f}. \quad (28)$$

With the initial condition  $D_f = 0$  for  $N = 0$ , one obtains  $C = -\alpha(D_f^{cr})^{\frac{1}{\alpha}}$ . In addition, for a given load the material fails after  $N = N_f$  loading cycles and the fatigue damage reaches its critical damage  $D_f^{cr}$ , it follows the relation among the plastic strain amplitude, the critical damage and the fatigue life  $N_f$ , as

$$\alpha(D_f^{cr})^{\frac{1}{\alpha}} = A(\epsilon_a^p)^{2n' - w + 1}(2N_f)^{1-w}. \quad (29)$$

It follows

$$B(2N_f)^{w-1} = (\epsilon_a^p)^{2n' - w + 1} \quad (30)$$

with

$$B = \frac{\alpha}{A}(D_f^{cr})^{\frac{1}{\alpha}}. \quad (31)$$

The power law relation between the plastic strain amplitude  $\Delta\epsilon_p$  and the fatigue life  $N_f$  is to be expressed as

$$\epsilon_a^p = \epsilon_f'(2N_f)^c, \quad (32)$$

where the fatigue exponent and fatigue strength coefficient can be related with the material parameters in the present fatigue damage model,  $\epsilon_f' = B^{1/(2n-w+1)}$  and  $c = (w-1)/(2n'-w+1)$ . Equation relates plastic strain amplitude as a loading parameter with a power-law function of the fatigue life  $N_f$ , which is the known Manson-Coffin model [28],

$$\epsilon_a = \epsilon_a^e + \epsilon_a^p = \frac{\sigma_f'}{E}(2N_f)^b + \epsilon_f'(2N_f)^c. \quad (33)$$

Above, the total applied strain amplitude is divided into elastic and plastic parts from the steady-state hysteresis loops.  $\sigma_f'$ ,  $\epsilon_f'$ ,  $b$  and  $c$  are fatigue strength coefficient, fatigue ductility coefficient, fatigue strength exponent and fatigue ductility exponent, respectively. From fatigue tests one can identify the model parameters for the Manson-Coffin model, as shown in Fig. 9, where the  $2N_f$  denotes the reversals to failure. From Eq. (32) one learns that the slope of Manson-Coffin equation in a log-log plot is determined by the material parameters  $w$  and  $n'$ .

The fatigue damage can be expressed as a function in number of cycles by integrating from  $N$  to  $N_f$  and  $D_f$  to  $D_f^{cr}$

$$\alpha(D_f^{cr})^{\frac{1}{\alpha}} \left(1 - \frac{D_f}{D_f^{cr}}\right)^{\frac{1}{\alpha}} = A(\epsilon_a^p)^{2n' - w + 1}(2N_f)^{1-w} \left[1 - \left(\frac{N}{N_f}\right)^{1-w}\right]. \quad (34)$$

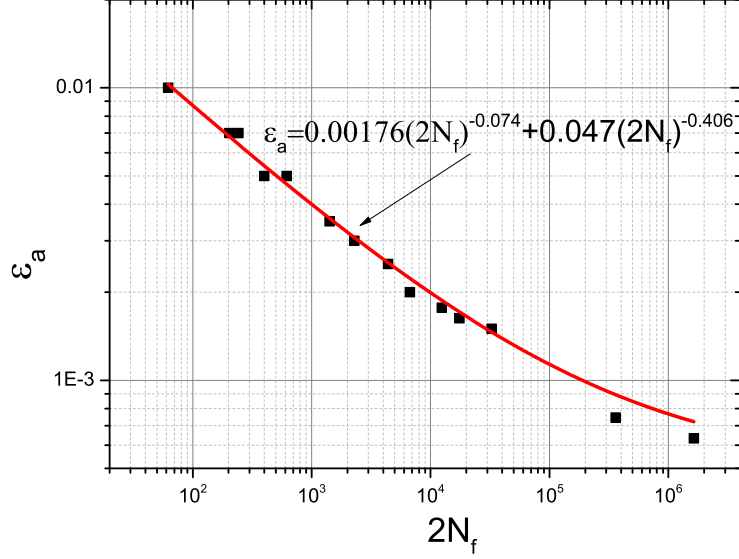


Figure 9. Total strain amplitude versus reversals to failure  $2N_f$  with uniaxial tension data.

Then, the relation between the normalized fatigue damage,  $D_f/D_f^{cr}$ , and the normalized number of cycles,  $N/N_f$ , under uniaxial loading can be expressed as

$$\frac{D_f}{D_f^{cr}} = 1 - \left[ 1 - \left( \frac{N}{N_f} \right)^{1-w} \right]^\alpha. \quad (35)$$

Figure 10 shows the parameter study of Eq. (35) to understand the effect of the material parameter  $\alpha$  on the form of the damage evolution law. It is found that the fatigue damage evolution law displays different shapes with different values of  $\alpha$ . For  $0 < \alpha < 1$ , the curve is concave which is the common form of the damage evolution in conventional dense metals [19]. In the case of  $\alpha > 1$  the respective shape of damage evolution is found in the brittle materials like concrete and rocks. The fatigue damage evolution of sintered metals in the present investigation shown in Fig. 5(b) displays the shapes with a mixed form, where  $0.25 < \alpha < 1$ . From Fig. 10 one may expect that the present damage evolution law is able to describe different fatigue behavior with different shapes of damage evolution curves. The related model parameters can be identified from the uniaxial fatigue tests.

## 5 Identification of model parameters

In the present work, a new damage model for fatigue has been developed in the framework of continuum damage mechanics. The proposed damage model can be used to predict the damage evolution in the sintered metals under both monotonic loading and fatigue loading. Additionally, the Ohno-Wang cyclic plasticity model is coupled with the damage model to describe cyclic deformation behavior. The identification process of material parameters is required for application of the proposed CDM model. The material parameters for monotonic loading cases

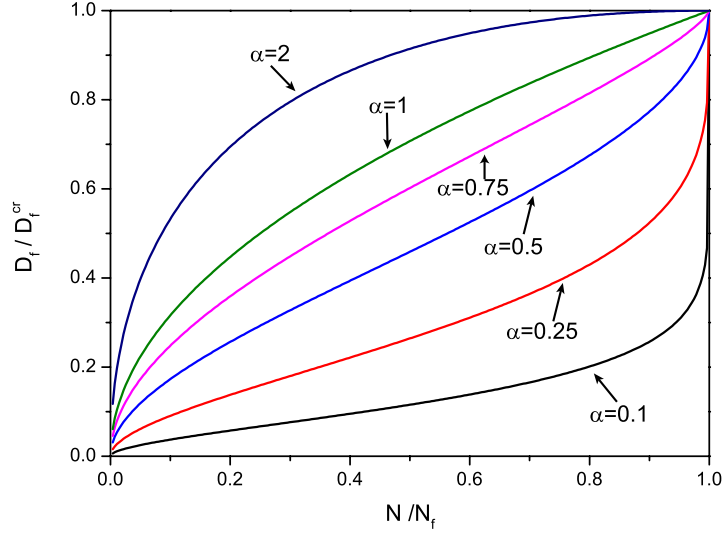


Figure 10. Effects of the model parameter  $\alpha$  in Eq. (35) to the shape of the damage evolution.

were discussed and identified in [21]. Therefore, this section will focus on the identification of material parameters of the fatigue damage law and cyclic plasticity model.

The fracture stress is  $\sigma_f = 258$  MPa in the monotonic tensile test. The material parameters  $w$  and  $S_f$  are calculated with the fatigue ductility exponent and fatigue strength coefficient in Eq. (33) by  $\epsilon'_f = B^{1/(2n-w+1)}$  and  $c = (w-1)/(2n'-w+1)$ ,  $w = 0.765$  and  $S_f = 2.6 \times 10^6$ . The material parameter  $\alpha$  is identified by fitting the data points of fatigue damage from the uniaxial test with the strain amplitude 0.003 using Eq. (35) as shown in Fig. 11,  $\alpha = 0.289$ . The critical damage  $D_f^{cr} = 0.18$  is directly obtained in Fig. 5(b).

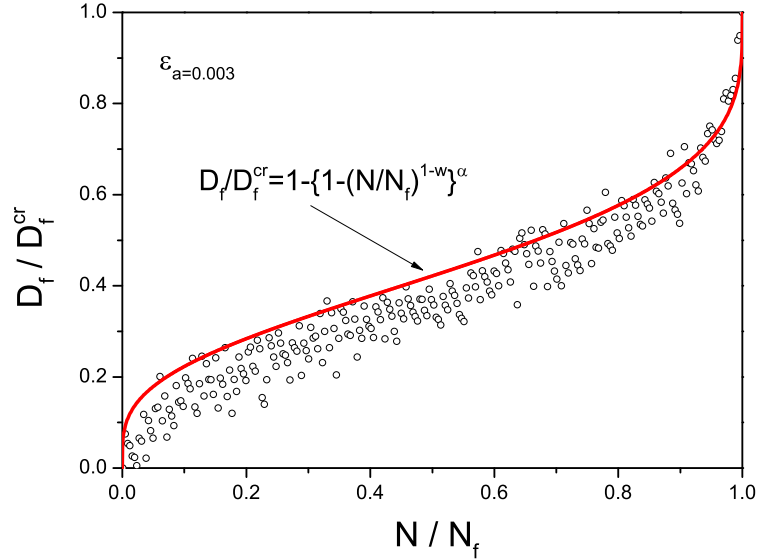


Figure 11. The material parameter  $\alpha$  is identified by fitting the data points of fatigue damage from uniaxial test of strain amplitude 0.003 using Eq. (35).

For the present damage model, the effective stress-strain curve is needed to describe the plastic behavior of the material. In Ohno-Wang's kinematic hardening rules, several linear hardening

Table 1

The material parameters for the Ohno-Wang's kinematic hardening rule identified with the stable uniaxial hysteresis curve of strain amplitude 0.01. (Unit: MPa)

$r_1 = 18$	$\zeta_1 = 33300$	$r_2 = 9$	$\zeta_2 = 13300$	$r_3 = 10$	$\zeta_3 = 7407$	$r_4 = 7$	$\zeta_4 = 4650$
$r_5 = 12$	$\zeta_5 = 3280$	$r_6 = 13$	$\zeta_6 = 2110$	$r_7 = 13$	$\zeta_7 = 1330$	$r_8 = 6$	$\zeta_8 = 819$
$r_9 = 3$	$\zeta_9 = 550$	$r_{10} = 3$	$\zeta_{10} = 459$	$r_{11} = 3$	$\zeta_{11} = 336$	$r_{12} = 11$	$\zeta_{12} = 263$
$r_{13} = 7$	$\zeta_{13} = 148$						

rules are employed to reproduce a nonlinear hysteresis curve. Several backstresses are used for the decomposition of the backstress in order to produce a good representation of the stable uniaxial hysteresis curve. In this study, 13 backstresses are found to be sufficient for obtaining a good stable loop simulation as shown in the simulation results. For each backstress  $\alpha_{ij}^{(k)}$ , two material parameters  $\zeta^{(k)}$  and  $r^{(k)}$  are required and determined by the following equations:

$$\zeta^{(k)} = \frac{\sigma^{(k)} - \sigma^{(k-1)}}{\epsilon^{p(k)} - \epsilon^{p(k-1)}} - \frac{\sigma^{(k+1)} - \sigma^{(k)}}{\epsilon^{p(k+1)} - \epsilon^{p(i)}} \quad (k \neq 1), \quad (36)$$

$$\gamma^{(k)} = \frac{2}{\epsilon^{p(k)} - \epsilon^{p(0)}} \quad (37)$$

$$r^{(k)} = \frac{\zeta^{(k)}}{\gamma^{(k)}} \quad (38)$$

Finally,  $\zeta^{(1)}$  can be determined with the equation  $\sum \frac{\zeta^{(k)}}{\gamma^{(k)}} + \sigma_0 = \sigma^0$ , where  $2\sigma_0$  is the size of the elastic range of the hysteresis curve. Totally, 26 material parameters are needed in Ohno-Wang's kinematic hardening rules. On the other hand, the stable cycle  $N_{sta}$  in the experiments is considered to be  $N_{sta} = 0.5N_f$ . The value  $N_{sta}/N_f = 0.5$  can be inserted into Eq. (35) to calculate the fatigue damage value  $D_f$  at  $N = N_{sta}$ , the elastic and plastic damage can be computer with plastic strain amplitude  $\Delta\epsilon_p$  and the stress amplitude  $\sigma_a$ , respectively. When the total damage is obtained, the undamaged hysteresis loop can be obtained from the experimental curve by  $\tilde{\sigma} = \sigma/(1 - D)$ , where  $D$  is assumed to be constant within one stable cycle. The material parameters for Ohno-Wang's kinematic hardening rule are identified with the stable uniaxial hysteresis curve of strain amplitude 0.01 and listed in Table. 1. The elastic properties can be found in [21] for the monotonic loading case. The initial yield stress  $\sigma_y$  is 135 MPa. The material parameter  $a$  in the equation of fatigue damage driving force can be calibrated with fatigue life from torsion and tension tests suggested by [15],  $a = 0.5$ .

## 6 Verification of damage evolution and fatigue life estimation

In this section the fatigue damage model calibrated with the uniaxial tests is applied for multi-axial fatigue with different strain amplitudes. Three loading paths, fully-reversed tension-

compression loading, cyclic torsion loading and proportional loading ( $\Delta\epsilon/\Delta\gamma = 1$ ), are employed for validating the proposed damage model (Fig. 12). For each loading path, four different strain amplitudes are considered,  $\epsilon_a^{eq} = 0.003, 0.005, 0.007, 0.01$ . Twelve loading cases are considered in verification of the proposed damage model.

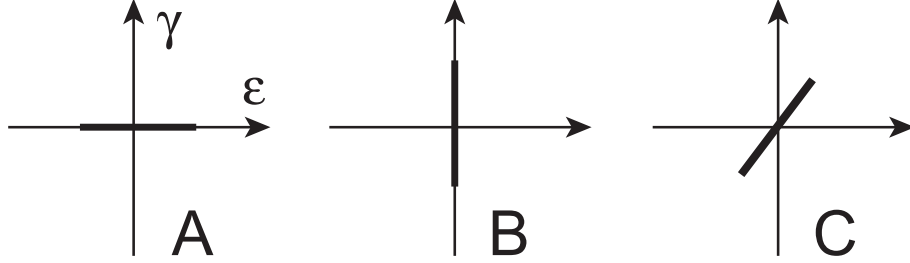


Figure 12. Thin-walled tubular specimens are subjected to three loading paths with different strain amplitudes to verify the damage model. A: tension; B: torsion; C: combined tension-torsion.

For the thin-walled tubular specimens, axisymmetric elements with twist, CGAX8, in ABAQUS are used for simulating the material response under tension-torsion loadings. The axial displacement and twist angle is applied to the upper edge of the specimen.

Fig. 13 presents comparison of the experimental stress-strain loops with computational results after stabilization. The half life cycle is defined as the stable cycle,  $N_{sta} = N_f/2$ , for computational results and experiments. Fig. 13(a) shows the results in the pure tension-compression cases. The points denote the experimental data. The solid lines represent the computational results. As discussed before, the material parameters for the Ohno-Wang's kinematic hardening rule were identified with the stable uniaxial hysteresis curve of strain amplitude 0.01. It is seen that the stress-strain loop in the computation meets the experimental data quite accurately. It is found in Fig. 13(a) that the proposed model overestimated the stress amplitude in other three loading cases. The reason is that the Ohno-Wang kinematic hardening law predicts the material response by using the Masing postulate, while the sintered iron displays non-Masing behavior in the experiments. On the other hand, the predicted elastic modulus in the unloading range of the stable cycle is in accordance with the experimental value for all loading cases. In Fig. 13(b) it is observed that the damage coupled cyclic plasticity model reasonably predicts the stress-strain response under torsion loading. Fig. 13(c) and (d) show the axial stress-axial strain and shear stress-shear strain loops of the stable cycle, respectively. The maximum stress is slightly underestimated in this case and under torsion loading.

More computational and experimental results are summarized in Fig. 14 for three different multi-axial paths: pure tension, pure torsion and tension-torsion. Figs. 14(a), (c) and (e) illustrate the development of damage in the course of loading, while Figs. 14(b), (d) and (f) show variations of the stress amplitudes in the specimens. In the figures the symbols denote experimental data. The solid lines represent computational results. It is seen that the fatigue damage evolution under torsion loading and proportional loading has similar shape as under uniaxial loading conditions. Additionally, the fatigue damage in the torsion cases grows more slowly than under tensile loading.

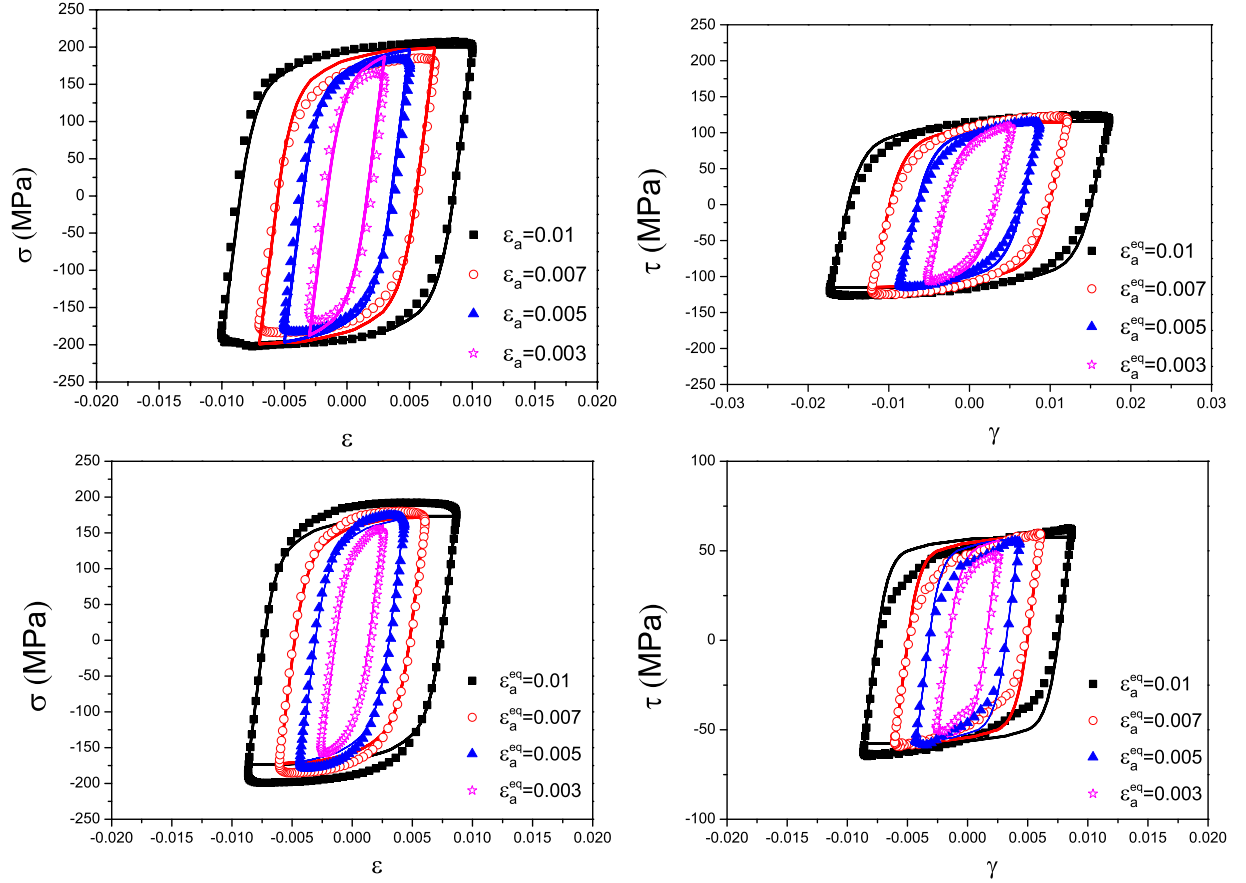
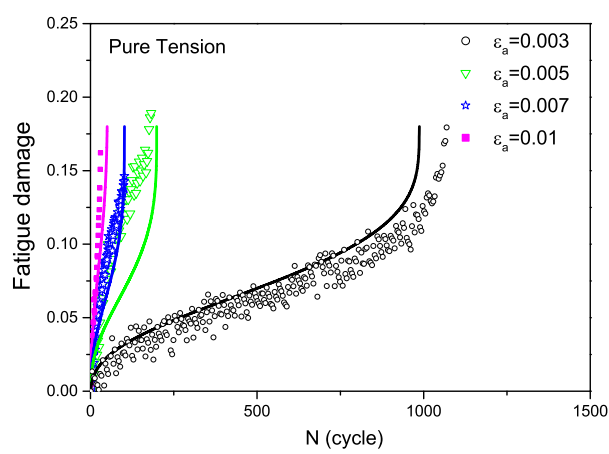


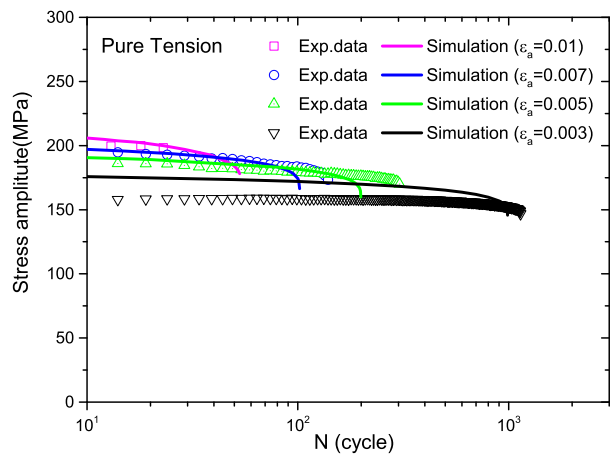
Figure 13. Comparison of experimental stress-strain loops with computational results in the stable cycles. ( $N_{sta}/N_f = 0.5$ )

Figures 14(b), (d) and (f) show the stress amplitude variation with the loading cycle in the experiments and simulations. In particular, the stress amplitude decreases rapidly at the final stage of fatigue life, where fatigue damage develops dramatically due to the coalescence of fatigue cracks. The simulation results show that the proposed damage model is able to predict the trend of stress amplitude variation for strain controlled loading paths. However, the simulation result overestimates the stress amplitude in the uniaxial loading case with  $\epsilon_a = 0.003$ , since the Ohno-Wang cyclic plasticity model overestimates the stress response in this case.

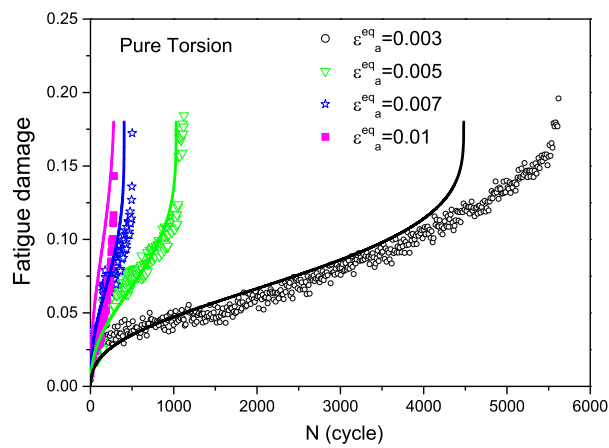
In fatigue life assessment one often compares the model predictions with experiments to quantify accuracy of the life prediction, as illustrated in Fig. 15. The solid line indicates accurate agreement between experiments and predictions. The two dotted lines are the factor-of-two boundaries. It is found that all of the data points fall within the factor-of-two lines. Generally, the prediction of the present fatigue damage evolution model is reasonable for the sintered iron under proportional loading condition. The detailed verification of the fatigue damage model should be continued under more complex loading conditions, i.e. non-proportional loading paths and variable amplitude loading cases.



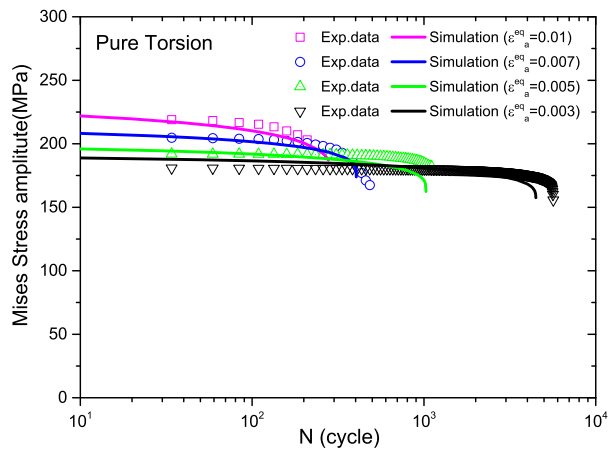
(a)



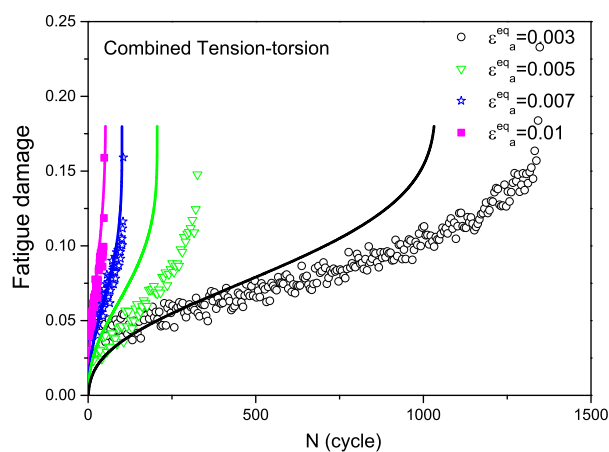
(b)



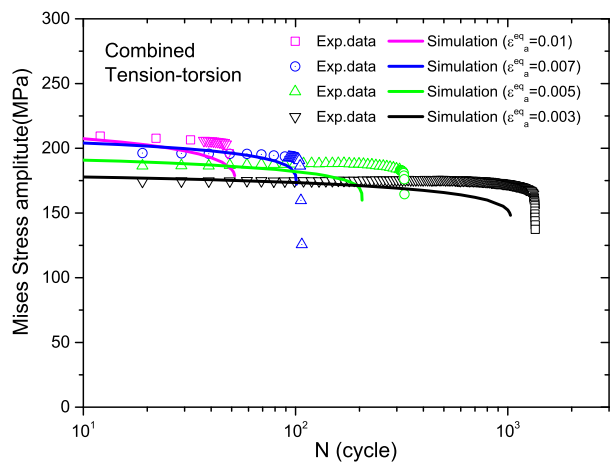
(c)



(d)



(e)



(f)

Figure 14. Comparison of the fatigue damage evolution and variation of the stress amplitudes between experimental and computational results under different cyclic loading paths.

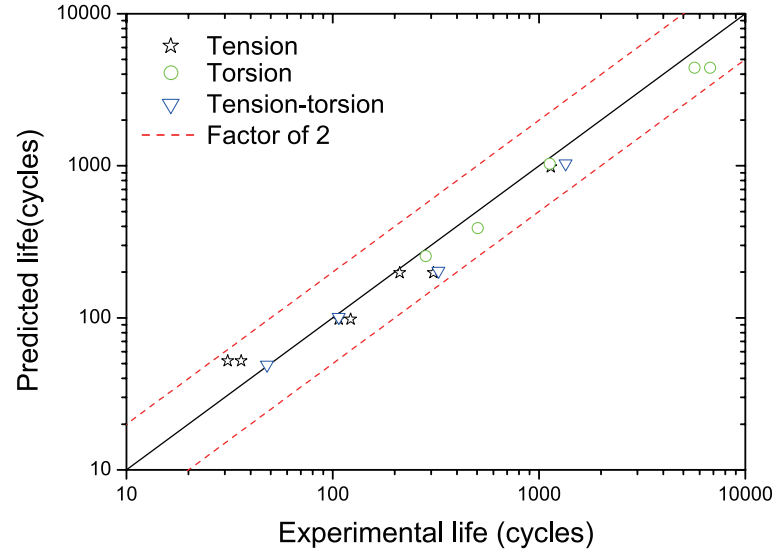


Figure 15. Comparison between experiments and predictions by the present continuum damage model under different cyclic loading paths and strain amplitudes.

## 7 Discussions and Conclusions

In the present work the multi-axial fatigue damage evolution in the porous sintered metal has been investigated experimentally and computationally. Based on detailed experimental observations, a new evolution equation for both elastic-plastic monotonic loading and fatigue damage has been established and embedded into cyclic plasticity. The implicit computational integration algorithm for the continuum damage mechanics model has been developed and implemented into the general purpose commercial finite element code ABAQUS. From the experimental and computational results the following conclusions can be drawn:

- The damage in sintered metal generally is decomposed into elastic-plastic damage and fatigue damage. The development of the sintered metal damage differs from conventional dense materials significantly and cannot be described by known damage models. The shape of the fatigue damage evolution curve in sintered metal is similar to that under monotonic loading. The fatigue damage development are characterized by three stages: The damage increases rapidly within the first few cycles, and then grows into a stable phase with loading cycles due to stable propagation of fatigue crack; finally, the damage develops dramatically and material loses its loading-capacity within few cycles, since micro cracks reach the critical crack length and material fails. Experiments shows that the development of the fatigue damage depends on loading amplitude and loading ratio.
- The material damage can be represented by the degradation of the material stiffness and consists of three parts: The elastic damage induced by micro-cracks in the sintered metal, the plastic damage caused by void initiation and growth during plastic deformations as well as the fatigue damage resulted from the subcritical crack growth under fluctuating loading. The elastic damage is mainly driven by the applied stress or the strain energy density, whereas the plastic damage is controlled by the plastic strain. The fatigue damage is essentially resulted from cyclic loading, represented by the accumulative plastic strain energy defined

on the critical plane. Three different damage evolution equations are proposed according to the experimental observation and calibrated by the experimental results.

- Most parameters in the constitutive model are identified from the uniaxial tests. Computational predictions are experimentally verified under different loading conditions. Generally, the prediction of the continuum fatigue damage model is reasonable for the sintered iron under proportional loading. The damage model coupled with cyclic plasticity generates reasonably the stress-strain response in the specimens under tension and torsion loading. However, the maximum stress is slightly underestimated under combined tension-torsion loading.
- The good agreement between the experimental results and the computational predictions establishes reliable basis for further validation of the present model for more complex loading cases. The present continuum damage model gives an accurate fatigue life prediction for all performed fatigue tests under multi-axial proportional loading conditions and possesses the potential to analyze more complex mechanical parts.

### **Acknowledgement:**

The present work is financed by the China Natural Science Foundation under the contract number 51175041. The authors thank the GKN Sinter Metals for providing the sintered metals and to Dr. Markus Schneider of GKN for the interesting discussions.

### **References**

- [1] B. Ayhan, P. Jehel, D. Brancherie, A. Ibrahimbegovic. Coupled damage–plasticity model for cyclic loading: Theoretical formulation and numerical implementation. *Engineering Structures* 50(2013) 30–42.
- [2] J. Baumgartner, K. Lipp, T. Bruder, and H. Kaufmann. Design methods for reliable fatigue assessment of PM components. *Materialwissenschaft und Werkstofftechnik* 42(2011) 894–903.
- [3] P. Beiss. *Pulvermetallurgische Fertigungstechnik*. Springer Verlag Berlin 2013.
- [4] N. Bonora, G.M. Newaz. Low cycle fatigue life estimation for ductile metals using a nonlinear continuum damage mechanics model. *International Journal of Solids and Structures* 35(1998) 1881–1894.
- [5] J. Cedergren, S. Melin, P. Lidström. Numerical modelling of p/m steel bars subjected to fatigue loading using an extended gurson model. *European Journal of Mechanics - A/Solids* 23(2004) 899–908.
- [6] J.L. Chaboche, P. M. Lesne. A non-linear continuous fatigue damage model. *Fatigue and Fracture of Engineering Materials and Structures* 11(1988) 1–17.
- [7] J.L. Chaboche, P. Kanouté, and F. Azzouz. Cyclic inelastic constitutive equations and their impact on the fatigue life predictions. *International Journal of Plasticity* 35(2012) 44–66.

- [8] G. Chen, X. Chen. Fatigue damage coupled constitutive model for 63Sn37Pb solder under proportional and non-proportional loading. *Mechanics of Materials* 39(2007) 11-23.
- [9] J. Chen, H. Yuan, M. Schneider. Investigation of micromechanical deformation mechanisms in sinter powder metals. *Advanced Material Research* 668(2013) 351–355.
- [10] X. Chen. On the Ohno-Wang kinematic hardening rules for multiaxial ratcheting modeling of medium carbon steel. *International Journal of Plasticity* 21(2005) 161–184.
- [11] X. Deng, G.B. Piotrowski, J.J. Williams, N. Chawla. Effect of porosity and tension-compression asymmetry on the bausinger effect in porous sintered steels. *International Journal of Fatigue* 27(2005) 1233–1243.
- [12] R. Desmorat, L. Angrand, P. Gaborit, M. Kaminski, C. Rakotoarisoa. On the introduction of a mean stress in kinetic damage evolution laws for fatigue. *International Journal of fatigue* 77 (2015) 141–153.
- [13] G. Glinka, G. Wang, A. Plumtree. Mean stress effects in multiaxial fatigue. *Fatigue and Fracture of Engineering Materials and Structures* 8(2007) 755–764.
- [14] R. Hojjati-Talemi, M.A. Wahab. Fretting fatigue crack initiation lifetime predictor tool: Using damage mechanics approach. *Tribology International* 60(2013) 176–186.
- [15] Y. Jiang. A fatigue criterion for general multiaxial loading. *Fatigue and Fracture of Engineering Materials and Structures* 23(2000) 19–32.
- [16] N. Khutia, P.P. Dey, S. Sivaprasad, S. Tarafder. Development of new cyclic plasticity model for 304LN stainless steel through simulation and experimental investigation. *Mechanics of Materials* 78(2014) 85–101.
- [17] O. Kintzel, S. Khan, J. Mosler. A novel isotropic quasi-brittle damage model applied to LCF analyses of AL2024. *International Journal of Fatigue* 32(2010) 1948–1959.
- [18] M. Kobayashi, N. Ohno. Implementation of cyclic plasticity models based on a general form of kinematic hardening. *International Journal for Numerical Methods in Engineering* 53(2002):2217–2238, 2002.
- [19] J. Lemaitre, R. Desmorat. *Engineering Damage Mechanics - Ductile, Creep, Fatigue and Brittle Failures*. Springer Verlag Berlin 2005.
- [20] B. Li, L. Reis, M. de Freitas. Comparative study of multiaxial fatigue damage models for ductile structural steels and brittle materials. *International Journal of Fatigue* 31(2009) 1895–1906.
- [21] S. Ma, H. Yuan. Damage evolution and modeling of sintered metals under multi-axial loading conditions. *Computational Materials Science* 80 (2013) 123–133.
- [22] S. Ma, H. Yuan. Computational investigation of multi-axial damage modeling for porous sintered metals with experimental verification. *Engineering Fracture Mechanics* 149 (2015) 89–110.
- [23] K. Marmi, M. Habraken, L. Duchene. Multiaxial fatigue damage modelling at macro scale of Ti–6Al–4V alloy. *International Journal of Fatigue* 31(2009) 2031–2040.
- [24] M. Naderi, M.M. Khonsari. An experimental approach to low-cycle fatigue damage based on thermodynamic entropy. *International Journal of Solids and Structures* 47(2010) 875–880.

- [25] M. Noban, H. Jahed, A. Varvani-farahani. The choice of cyclic plasticity models in fatigue life assessment of 304 and 1045 steel alloys based on the critical plane-energy fatigue damage approach. *International Journal of Fatigue* 43(2012) 217–225.
- [26] M. Schneider. Deformation and low-cycle fatigue of sintered iron and steels. PhD thesis, University of Wuppertal, Department of Mechanical Engineering, 2013.
- [27] M. Schneider, H. Yuan. Experimental and computational investigation of cyclic mechanical behavior of sintered iron. *Computational Materials Science* 57(2012) 48–58.
- [28] D.F. Socie, G.B. Marquis. Multiaxial Fatigue. Society of Automotive Engineers, Inc. Warrendale 2000.
- [29] C.M. Sonsino. Fatigue design principles for sintered steel components. *The Journal of Strain Analysis for Engineering Design* 41(2006) 497–555.
- [30] G. Straffelini and A. Molinari. Evolution of tensile damage in porous iron. *Materials Science and Engineering: A* 334(2002) 96–103.
- [31] M. Vormwald, R. Döring. Deformations and damage to metallic materials under multiaxial non-proportional loading. *Computational Materials Science* 46(2009) 555–560.
- [32] Q. Yu, J. Zhang, Y. Jiang, Q. Li. Multiaxial fatigue of extruded AZ61A magnesium alloy. *International Journal of Fatigue* 33(2011) 437–447.
- [33] H. Yuan, S. Ma, L. Zhang. Continuum damage mechanics for sintered powder metals. *Science China Physics, Mechanics & Astronomy* 58(2015) 1–12.
- [34] A. Zafari, P. Beiss. Effect of tensile mean stresses on fatigue strength of fe-cu-c steels in as-sintered and heat treated conditions. *Powder Metallurgy Progress* 8(2008) 200–209.
- [35] K.-S. Zhang, J.W. Ju, Z. Li, Y.-L. Bai, W. Brocks. Micromechanics based fatigue life prediction of a polycrystalline metal applying crystal plasticity. *Mechanics of Materials* 85(2015) 16-37.